The Astrophysical Journal, 834:60 (15pp), 2017 January 1 doi:10.3847/1538-4357/834/1/60

INTERSTELLAR-MEDIUM MAPPING IN M82 THROUGH LIGHT ECHOES AROUND SUPERNOVA 2014J

Yi Yang[1], Lifan Wang[1,2], Dietrich Baade[3], Peter. J. Brown[1], Misty Cracraft[4], Peter A. Höflich[5], Justyn Maund[6], Ferdinando Patat[3], William B. Sparks[4], Jason Spyromilio[3], Heloise F. Stevance[6], Xiaofeng Wang[7], and J. Craig Wheeler[8]

[1] George P. and Cynthia Woods Mitchell Institute for Fundamental Physics & Astronomy, Texas A. & M. University, Department of Physics and Astronomy, 4242 TAMU, College Station, TX 77843, USA; ngc4594@physics.tamu.edu
[2] Purple Mountain Observatory, Chinese Academy of Sciences, Nanjing 210008, China
[3] European Organisation for Astronomical Research in the Southern Hemisphere (ESO), Karl-Schwarzschild-Straße 2, D-85748 Garching b. München, Germany
[4] Space Telescope Science Institute, Baltimore, MD 21218, USA
[5] Department of Physics, Florida State University, Tallahassee, Florida 32306-4350, USA
[6] Department of Physics and Astronomy, University of Sheffield, Hicks Building, Hounsfield Road, Sheffield S3 7RH, UK
[7] Physics Department and Tsinghua Center for Astrophysics (THCA), Tsinghua University, Beijing, 100084, China
[8] Department of Astronomy and McDonald Observatory, The University of Texas at Austin, Austin, TX 78712, USA
Received 2016 September 30; revised 2016 November 7; accepted 2016 November 7; published 2017 January 3

ABSTRACT

We present multiple-epoch measurements of the size and surface brightness of the light echoes from supernova (SN) 2014J in the nearby starburst galaxy M82. *Hubble Space Telescope* (*HST*) ACS/WFC images were taken ∼277 and ∼416 days after *B*-band maximum in the filters *F475W*, *F606W*, and *F775W*. Observations with *HST* WFC3/UVIS images at epochs ∼216 and ∼365 days are included for a more complete analysis. The images reveal the temporal evolution of at least two major light-echo components. The first one exhibits a filled ring structure with position-angle-dependent intensity. This radially extended, diffuse echo indicates the presence of an inhomogeneous interstellar dust cloud ranging from ∼100 to ∼500 pc in the foreground of the SN. The second echo component appears as an unresolved luminous quarter-circle arc centered on the SN. The wavelength dependence of scattering measured in different dust components suggests that the dust producing the luminous arc favors smaller grain sizes, while that causing the diffuse light echo may have sizes similar to those of the Milky Way dust. Smaller grains can produce an optical depth consistent with that along the supernova-Earth line of sight measured by previous studies around maximum light. Therefore, it is possible that the dust slab from which the luminous arc arises is also responsible for most of the extinction toward SN 2014J. The optical depths determined from the Milky Way-like dust in the scattering matters are lower than the optical depth produced by the dust slab.

Key words: circumstellar matter – dust, extinction – galaxies: individual (M82) – ISM: structure – polarization – supernovae: individual (SN 2014J)

Supporting material: extended figures

1. INTRODUCTION

Interstellar extinction caused by dust affects most astronomical observations. Light traversing a certain distribution of interstellar medium (ISM) produces an integrated effect on extinction. Extinction traces the dust grains, but also diminishes the starlight and limits our ability to interpret the local and distant universe. The study of interstellar dust provides insight into the properties of the extinction. Since dust is a strong coolant, it also plays a critical role in controlling galaxy evolution and star formation.

Observations of interstellar extinction require a beacon shining through interstellar material. In the Milky Way, a very large number of sightlines are available for this purpose, while in external galaxies there are few point source beacons bright enough to study the local ISM. Supernovae (SNe) are the best, and often only, choice. Light echoes provide additional information because they literally reflect light-scattering properties and do not reach the observer along exactly the same path. If SNe are nearby, even resolved light echoes may be observable.

The extinction (in magnitudes) at a certain wavelength or bandpass, λ, is often expressed as $A_\lambda = R_\lambda \times E(B-V)$. The "total-to-selective" extinction $R_V = A_V/E(B-V)$ depends on the properties of the dust along the line of sight and can be derived by comparing the observed $E(\lambda - V)$ with the extinction curves given by Cardelli et al. (1989). The observed wavelength dependence of interstellar extinction contains information on both the size and composition of the grains. The value of $R_V = 3.1$ (Cardelli et al. 1989) has often been considered the Galactic standard, but with a range from 2.2 to 5.8 (Fitzpatrick 1999) for different lines of sight. There is increasing evidence that extinction curves toward SNe Ia exhibit a steeper wavelength dependence ($R_V < 3$, see Cikota et al. 2016 for a summary on R_V results of earlier studies). Patat et al. (2007) reported the detection of circumstellar material (CSM) in the local environment surrounding the SN Ia SN 2006X in the nearby galaxy M100. Wang (2005), Patat et al. (2006), and Goobar (2008) showed that the scattered light from CSM tends to reduce the value of R_λ in the optical. The effect on R_V and the light-curve shape, however, also depends on the geometrical configuration and dust-grain properties (Amanullah & Goobar 2011; Brown et al. 2015). It is of critical importance to understand whether the low R_V values are caused by (1) systematic differences from extragalactic environments, (2) inhomogeneities in the vicinity of the SN-Earth direct line of sight (DLOS), or (3) modifications by CSM scattering.

The most reliable approach in determining the extinction is the "pair method"—comparing spectrophotometry of two sources with the same spectral energy distribution, one of which has negligible foreground extinction. Extragalactic reddening can be

Table 1
Spatially Resolved Supernova Light Echoes

SN	Type	Host Galaxy	Distance (Mpc)	References
1987A	II-Peculiar	LMC	0.05	1, 3, 16, 17, 23
1991T	Ia 91T-like	NGC 4527	15.2	11, 12
1993J	IIb	M81	3.6	6, 13
1995E	Ia	NGC 2441	49.6	10
1998bu	Ia	M96	9.9	2
1999ev	II-P	NGC 4274	9.9	7
2002hh	II-P	NGC 6946	5.5	8, 22
2003gd	II-P	M74	9.5	14, 18
2004et	II-P	NGC 6946	5.5	9
2006X	Ia	M100	15.9	21
2007af	Ia	NGC 5584	22.5	5
2008bk	II-P	NGC 7793	3.7	19
2012aw	II-P	M95	10.0	20
2014J	Ia	M82	3.5	4
2016adj	IIb	NGC 5128	3.7	15

References. (1) Bond et al. (1990), (2) Cappellaro et al. (2001), (3) Crotts (1988), (4) Crotts (2015), (5) Drozdov et al. (2015), (6) Liu et al. (2003), (7) Maund & Smartt (2005), (8) Meikle et al. (2006), (9) Otsuka et al. (2012), (10) Quinn et al. (2006), (11) Schmidt et al. (1994), (12) Sparks et al. (1999), (13) Sugerman & Crotts (2002), (14) Sugerman (2005), (15) Sugerman & Lawrence (2016), (16) Suntzeff et al. (1988), (17) Spyromilio et al. (1995), (18) Van Dyk et al. (2006), (19) Van Dyk (2013), (20) Van Dyk et al. (2015), (21) Wang et al. (2008), (22) Welch et al. (2007), (23) Xu et al. (1994).

measured by comparing observed SNe Ia to a zero-reddening locus (e.g., Riess et al. 1996; Phillips et al. 1999). However, information acquired through this pair method is limited to single sightlines. Photons scattered by dust travel a slightly different path compared to the directly transmitted light. Therefore, scattered photons provide chances to test the scattering properties of the dust in a bidimensional space.

1.1. Light Echoes

Light echoes are the scattered light of a transient event that arise from dust clouds. Here we consider the case of an SN and CSM/ISM. Because of the high initial brightness of SNe, searches for late-time off-source flux excesses have been the main approaches to detect light echoes residing close to the SNe, i.e., the slowly fading light-curves of SN 1991T (Schmidt et al. 1994; Sparks et al. 1999), SN 1998bu (Cappellaro et al. 2001), and SN 2006X (Wang et al. 2008). Outside the solar system, spatially resolved light echoes have been rare events. The first one reported arose around Nova Persei 1901 (Kapteyn 1901; Ritchey 1901), followed by Nova Sagittarii 1936 (Swope 1940). Echoes were also found from the Galactic Cepheid RS Puppis (Havlen 1972) and, with *Hubble Space Telescope* (*HST*) angular sampling, from the eruptive star V838 Monocerotis (Bond et al. 2003). Vogt et al. (2012) reported the detection of an infrared echo near the Galactic supernova remnant Cassiopeia A. Additionally, spectroscopic observations of nearby light echoes provide unique opportunities to probe the progenitor properties of historical transients (Rest et al. 2008; Davidson & Humphreys 2012) and in some cases the three-dimenisonal structure of the explosion, for instance, an ancient eruption from η Carinae (Rest et al. 2012), or asymmetry in the outburst of SN 1987A (Sinnott et al. 2013) and Cassiopeia A (Grefenstette et al. 2014). In recent years, the number of light echoes from extragalactic SNe has grown rapidly, mostly thanks to *HST*. Table 1 provides an overview of the events recorded to date, updated from Table 1 of Van Dyk et al. (2015).

Photons from spatially resolved light echoes travel a slightly different path than the DLOS from the SN to Earth. Therefore, observations of a resolved light echo around a nearby SN provide a unique opportunity to measure the extinction properties of the dust along the DLOS and the scattering properties of the echo-producing dust independently and simultaneously. As the SN fades, outer echoes (echoes with larger angular diameter) associated with ISM at large distances to the SN will become less contaminated by its bright light, and any inner echoes associated with ISM at small distances to the SN, and even the CSM, will become detectable. The expansion with time of the light echoes maps out the 3D structure of ISM along and close to the line of sight.

Detailed introductions to the relation between two-dimensional light echoes and three-dimensional scattering dust distributions has been given in various studies (Chevalier 1986; Sparks 1994; Sugerman 2003; Tylenda 2004; Patat 2005). Here, we briefly define the geometry used throughout this paper, also shown in Figure 1, which considers the SN event as an instantaneous flash of radiation. The locus of constant light travel time is an ellipsoid with the supernova at one focus, which we refer to as an iso-delay surface. The ellipsoid grows with time as the light propagates in space.

The angular radius of the light echo (α) can be easily measured in two-dimensional images. The SN is centered at the origin of the plane, the x and y give the coordinates of the scattering materials in the plane of the sky. The projected distance ($\rho = \sqrt{x^2 + y^2}$) of scattering material to the SN perpendicular to the DLOS is related to the distance (D) to the SN as $\tan\alpha = \rho/D$, ϕ gives the position angle (PA). Because D is significantly larger than other geometric dimensions, the light echo can be very well approximated by a paraboloid, with the SN lying at its focus. ρ can be obtained by

$$\rho = \sqrt{ct\,(2z + ct)}\,. \tag{1}$$

Here t is the time since the radiation burst, z gives the foreground distance of the scattering material along the line of sight, and c denotes the speed of light. The distance r of the scattering material from the SN is

$$r = \frac{1}{2}\left(\frac{\rho^2}{ct} + ct\right). \tag{2}$$

The scattering angle can be obtained from $\cos\theta(\rho, t) = z/(z + ct)$ or from $\tan\theta = \rho/z$.

1.2. Supernova 2014J in M82

The nearby SN Ia 2014J in M82 (3.53 ± 0.04 Mpc, Dalcanton et al. 2009) offers the rare opportunity to study the physical properties and spatial distribution of dust particles along *and close to* the DLOS and also in the vicinity of the SN. SN 2014J suffers from heavy extinction ($A_V = 2.07 \pm 0.18$, Foley et al. 2014) and is located behind a large amount of interstellar dust (Amanullah et al. 2014). Additionally, the absorption profiles of Na and K lines from high-resolution spectroscopy exhibit more than ten extragalactic absorption components, indicating that the extinction along the DLOS is caused by the combined presence of a large number of distinct interstellar dust clouds along the DLOS (Patat et al. 2015). SN 2014J was discovered on January 21.805 UT by Fossey

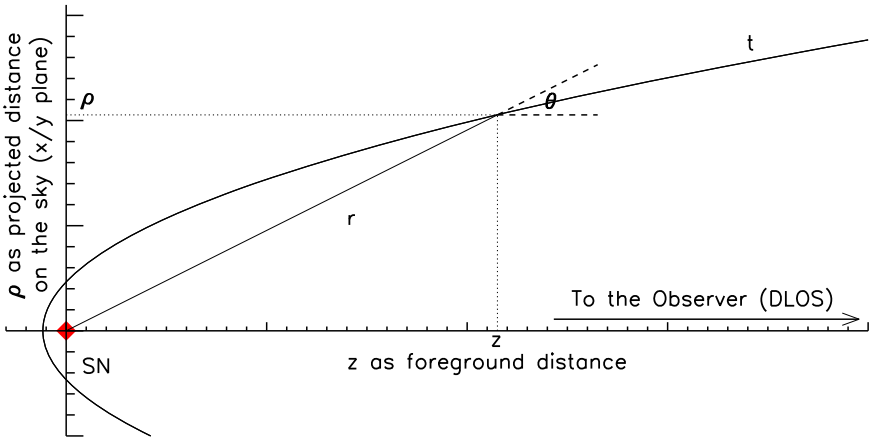

Figure 1. Schematic diagram identifying the geometrical parameters used in this paper. The paraboloid represents the iso-delay light surface at some arbitrary epoch after the supernova explosion. The observer located along the z-axis and beyond the right edge of the diagram would see light echoes in the x–y plane (the y is perpendicular to the drawing). The SN is located at the origin, and θ denotes the scattering angle.

et al. (2014). Later observations constrained the first light of the SN to January 14.75 UT (Goobar et al. 2014; Zheng et al. 2014).

SN 2014J reached its B-band maximum on February 2.0 UT (JD 2,456,690.5) at a mgnitude of 11.85 ± 0.02 (Foley et al. 2014). Continuous photometric and spectroscopic observations through late phases have been made by various groups (Johansson et al. 2014; Lundqvist et al. 2015; Bonanos & Boumis 2016; Porter et al. 2016; Sand et al. 2016; Srivastav et al. 2016).

There is clear evidence that the strong extinction measured from SN 2014J is caused primarily by interstellar dust (Brown et al. 2015; Patat et al. 2015), although a mix of interstellar and circumstellar dust is also possible (Foley et al. 2014; Bulla et al. 2016). Several independent studies, including photometric color fitting from *Swift*/UVOT and *HST* (Amanullah et al. 2014), near-UV/optical grism spectroscopy from *Swift* UVOT (Brown et al. 2015), *HST* STIS spectroscopy and WFC3 photometry (Foley et al. 2014), reddening curve fitting near the SN maximum using the silicate-graphite model (Gao et al. 2015), as well as optical spectroscopy from Goobar et al. (2014) found an $R_V \sim 1.4$ toward SN 2014J. Moreover, ground-based broadband imaging polarimetry (Kawabata et al. 2014; Srivastav et al. 2016) and spectropolarimetry (Patat et al. 2015; Porter et al. 2016) have shown that the polarization peak that is due to interstellar dust extinction is shortward of $\sim$0.4 μm, which indicates that this line of sight has peculiar Serkowski parameters (see Patat et al. 2015). This polarization wavelength dependence can be interpreted in terms of a significantly enhanced abundance of small grains (Patat et al. 2015). Models considering both interstellar dust and circumstellar dust simultaneously and fitted to observed extinction and polarization (Hoang 2015) find that a significant enhancement (w.r.t. the Milky Way) in the total mass of small grains ($<$0.1 μm) is required to reproduce low values of R_V. Multiple time-invariant Na I D and Ca II H&K absorption features as well as several diffuse interstellar bands have also been identified (Graham et al. 2015; Jack et al. 2015). These are most likely associated with multiple dust components of interstellar material along the DLOS.

The nature (amount and distribution) of CSM is of interest when probing the possible diversity of progenitors of SNe Ia and for accurately correcting the extinction when using SNe Ia as standard candles. Johansson et al. (2014) found no evidence of heated dust in the CSM of SN 2014J with $r < 10^{17}$ cm ($\sim$39 light days). Graham et al. (2015) reported variable interstellar K I lines in high-resolution spectra, which may form about 10 light years ($\sim 10^{19}$ cm) in front of the SN.

The extremely dusty environment in M82 and its relative proximity to Earth lead to the expectation of complex and evolving light echoes if SN 2014J exploded inside the galactic disk. In fact, Crotts (2015) discovered the first light echoes surrounding SN 2014J in *HST* images from 2014 September 5, 215.8 days past B-band maximum light (referred to as +216 d hereafter) on JD = 2456690.5 (Foley et al. 2014). The echo signal tends to be associated with pre-explosion nebular structures in M82 (Crotts 2015).

In the following, we present the evolution of multiple light echoes of SN 2014J as revealed by new *HST* ACS/WFC multiband and multi-epoch imaging around $\sim$277 days and $\sim$416 days past B-band maximum (referred to as +277 d and +416 d below). We also qualitatively discuss similar archival WFC3/UVIS images obtained on +216 d and +365 d.

2. OBSERVATIONS AND DATA REDUCTION

Late-time observations of the light echoes around SN 2014J discussed in this paper result from a *HST* Wide Field Camera 3 UVIS channel (*HST* WFC3/UVIS) program (#13626; PI: Crotts) to observe properties of the light echoes and progenitor environment around SN 2014J and an Advanced Camera for Surveys/Wide Field Channel (*HST* ACS/WFC) program (#13717; PI: Wang) to probe the dusty environment surrounding SN 2014J in M82. A log of observations is assembled in Table 2.

We use bright H II regions to align exposures in different filter combinations and epochs through *Tweakreg* in the *Astrodrizzle* package (Gonzaga et al. 2012). Observations obtained with three polarizers are needed to calculate the Stokes vectors, but the intensity maps (Stokes I) are the only input to this analysis.

$$I = \frac{2}{3}[r\,(\mathrm{POL0}) + r\,(\mathrm{POL60}) + r\,(\mathrm{POL120})], \qquad (3)$$

where r(POL0), etc. are the count rates in the images obtained through the three polarizers. Figure 2 shows the field around SN 2014J.

Table 2
Log of Observations of SN 2014J with *HST* WFC3/UVIS and ACS/WFC POLV

HST Camera	Filter	Polarizer	Date of 1st Obs. (UT-2014)	Exp. Time (s)	Epoch[a] (Days)	Date of 2nd Obs. (UT-2015)	Exp. Time (s)	Epoch[a] (Days)
WFC3/UVIS[b]	*F438W*	N/A	09-05 19:12:57	8 × 64	215.8	02-02 05:24:41	12 × 128	365.2
	F555W	N/A	09-05 19:29:44	4 × 64	215.8	02-02 05:06:06	12 × 32	365.2
	F555W	N/A	09-05 22:05:11	8 × 32	215.9	N/A	N/A	N/A
	F814W	N/A	09-05 20:32:05	8 × 64	215.9	N/A	N/A	N/A
ACS/WFC[c]	*F475W*	POL0V	11-06 00:24:42	3 × 130	276.5	03-25 01:56:17	3 × 400	415.6
	F475W	POL120V	11-06 00:42:24	3 × 130	276.5	03-25 03:22:43	3 × 400	415.6
	F475W	POL60V	11-06 01:00:03	3 × 130	276.5	03-25 03:53:40	3 × 400	415.7
	F606W	POL0V	11-06 01:18:11	2 × 40	276.6	03-27 10:17:38	3 × 60	417.9
	F606W	POL120V	11-06 01:59:48	2 × 40	276.6	03-27 11:10:48	3 × 60	418.0
	F606W	POL60V	11-06 02:13:58	2 × 40	276.6	03-27 11:30:17	3 × 60	418.0
	F775W	POL0V	11-06 02:23:28	2 × 30	276.6	03-27 11:50:26	3 × 20	418.0
	F775W	POL120V	11-06 02:37:21	1 × 55	276.6	03-27 12:58:00	3 × 20	418.0
	F775W	POL60V	11-06 02:41:46	1 × 55	276.6	03-27 13:02:17	3 × 20	418.0

Notes.
[a] Days after B maximum on 2014 February 2.0 (JD 2 456 690.5).
[b] Observations result from *HST* WFC3/UVIS, program (#13626; PI: Crotts).
[c] Observations result from *HST* ACS/WFC, program (#13717; PI: Wang).

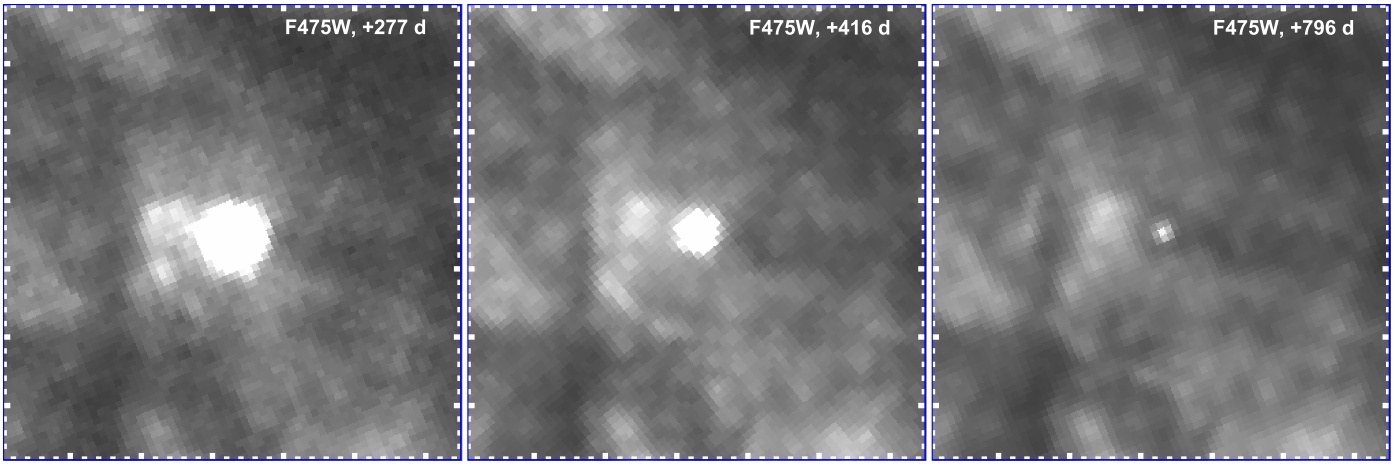

Figure 2. *HST* ACS/WFC *F475W* images of SN 2014J obtained at different epochs as labeled. Each square measures $3\farcs2 = 54$ pc along its sides (north is up, east is left). The distance between little tick marks corresponds to $0\farcs1$.

We perform background subtraction to better reveal the faint and time-variant light-echo signals. For observations on +277 d and +416 d with *HST* ACS/WFC and filters *F475W*, *F606W*, and *F775W*, we found no pre-SN *Hubble* images of the region through filters consistent with our observations. The most recent *HST* images of SN 2014J obtained on 2016 April 8, (+796 d) with the same photometric and polarimetric filter combinations were subtracted from the observations on +277 d and +416 d. For the observations on +216 d and +365 d with *HST* WFC3/UVIS in passbands *F438W*, *F555W*, and *F814W*, pre-SN images obtained on 2006 March 29 (program #10776; PI:Mountain) with *HST* ACS/WFC in the *F435W*, *F555W*, and *F814W* were used as background templates, respectively. For each band, the background templates were scaled and subtracted from the intensity map.

The resulting images (Figure 3) clearly reveal the shape of the light echoes around SN 2014J. Negative signals (black in Figure 3) represent the light echoes on +796 d, while positive (white) signals trace the light echoes on +277 d and +416 d, respectively. In each subpanel of Figure 3, we show the light echoes with background removed (labeled "Image" at the bottom), the scaled and distortion-corrected point-spread function (PSF) (labeled "PSF" on the left), and the residual around the SN after PSF subtraction (labeled "Res" on the right). PSF appropriate to the SN position were generated for each bandpass and epoch with TinyTim (Krist 1993; Krist & Hook 2008). The upper row displays the observations at earlier epochs (+216 d for *F438W* and *F555W*, +277 d for *F475W*, *F606W*, and *F775W*), and the lower row depicts the observations at later epochs (+365 d for *F438W* and *F555W*, +416 d for *F475W*, *F606W*, and *F775W*). For better visibility, Figure 4 provides a zoom-in of the PSF-subtracted images ("Res") in each panel of Figure 3.

3. ANALYSIS AND RESULTS

3.1. Total Flux of the SN

Photometry of SN 2014J at four epochs was performed in the background-subtracted images described above, and shown in Table 3. Measurements were made with a circular aperture of

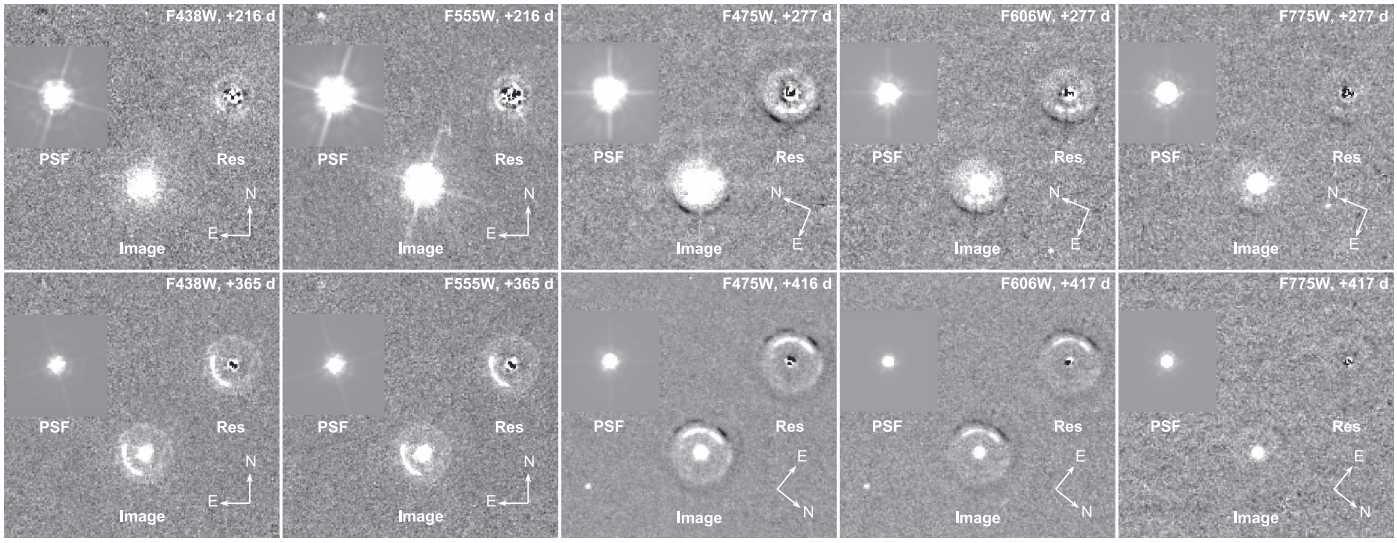

Figure 3. Background-subtracted images of the SN ("Image"), the TinyTim PSF (Krist 1993; Krist & Hook 2008), and the residuals around the SN after PSF subtraction ("Res"). Background structures in *F*438*W* and *F*555*W* were removed by subtracting scaled pre-SN archival *F*435*W* and *F*555*W HST* images. Background in *F*475*W*, *F*606*W*, and *F*775*W* was corrected for by subtracting the respective most recent +796 d image; therefore, the +796 d echoes appear as negative structures. Note the different orientations.

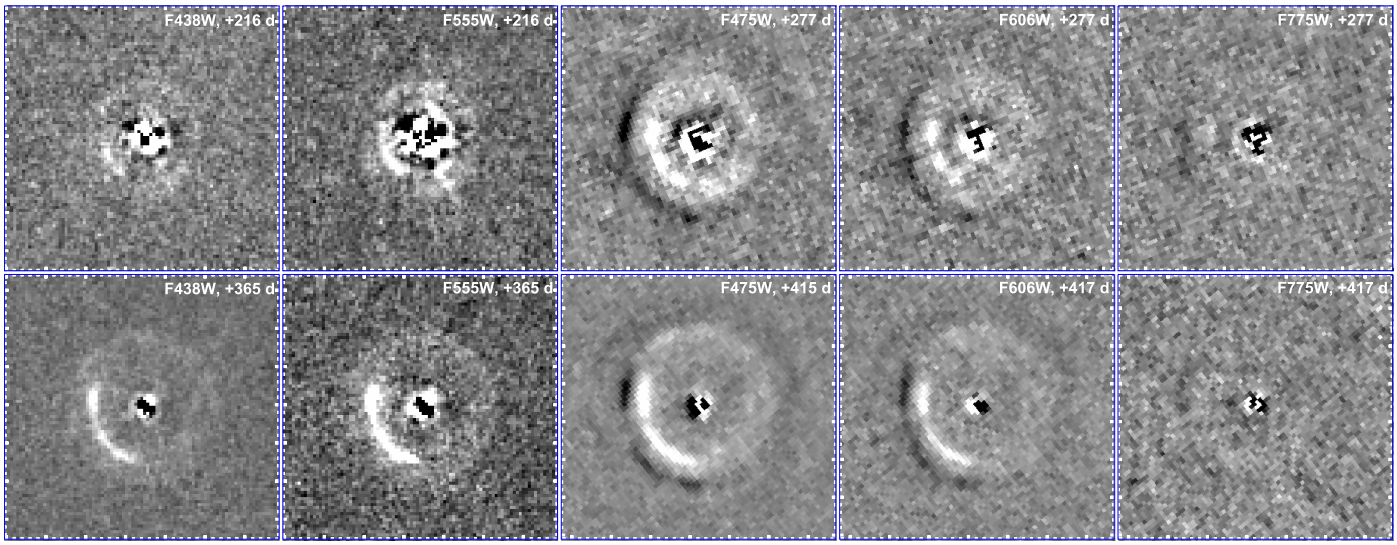

Figure 4. A zoom-in view of the background-corrected light echoes shown in Figure 3. North is up and east is left. The distance between each little tickmark is $0\farcs1$. Each square measures $3\farcs4 = 58$ pc along its sides. The diffuse and radially extended light-echo profiles can be clearly identified in all panels except for *F*438*W* (+216 d) and *F*775*W* (all epochs). Note the uneven signal distribution with position angle in the rings and the consistency of the overall patterns at different epochs. A luminous arc is visible in the lower left quadrant and not resolved in the radial direction. This is at variance with the appearance of the complete, radially diffuse rings.

Table 3
HST Photometry of SN 2014J and Light Echoes (Total Echo Profile)

t[a]	$F438W_{SN}$	$F555W_{SN}$	$F814W_{SN}$	$F438W_{LE}$	$F555W_{LE}$
215.8	17.610 ± 0.016	16.446 ± 0.011	15.301 ± 0.011	22.05 ± 0.36	21.12 ± 0.06
365.3	19.735 ± 0.011	18.715 ± 0.013	N/A[b]	21.53 ± 0.13	20.87 ± 0.06
t[a]	$F475W_{SN}$	$F606W_{SN}$	$F775W_{SN}$	$F475W_{LE}$	$F606W_{LE}$
276.5	17.467 ± 0.002	17.343 ± 0.002	16.354 ± 0.005	21.16 ± 0.03	20.73 ± 0.08
415.6[c]	19.568 ± 0.002	19.516 ± 0.004	17.888 ± 0.008	21.37 ± 0.02	20.98 ± 0.05

Notes.
[a] Days after *B* maximum, 2014 February 2.0 (JD 245 6690.5).
[b] SN 2014J was not observed in *F*814*W* at +365 d.
[c] +417.9 d for *F*606*W*, +418.0 d for *F*775*W*.

Table 4
Geometric Properties of (Unresolved) Luminous-arc Light-echo (LE) Components

LE #	Epoch[a] (Day)	Angular Radius α ($''$)	Offset ($''$)	Foreground Distance z (pc)	Projected Radius ρ (pc)	Scattering Angle θ (°)
Arc	215.8	0.539 ± 0.020	0.009 ± 0.014	234.6 ± 18.2	9.22 ± 0.36	2.25 ± 0.20
	276.5	0.599 ± 0.014	0.006 ± 0.015	226.3 ± 11.8	10.25 ± 0.27	2.60 ± 0.15
	365.3	0.689 ± 0.020	0.011 ± 0.014	226.4 ± 14.1	11.79 ± 0.37	2.98 ± 0.21
	415.6	0.735 ± 0.012	0.012 ± 0.010	226.6 ± 9.0	12.58 ± 0.25	3.18 ± 0.14

Note.
[a] Days after B maximum on 2014 February 2.0 (JD 245 6690.5).

$0\farcs4$ (8 pixels in the ACS/WFC FOV and 10 pixels in the WFC3/UVIS FOV) in the WFC3/UVIS $F438W$, $F555W$, $F814W$ images from +216 d, and the $F438W$ and $F555W$ images from +365 d. We applied aperture corrections according to Hartig (2009) and Sirianni et al. (2005) to estimate the total flux from SN 2014J. The photometric uncertainties in Table 3 include the Poisson noise of the signal, the photon noise of the background, the readout noise contribution (3.75 electrons/pixel for ACS/WFC), and the uncertainties in aperture corrections. These quantities were added in quadrature. The magnitudes are presented in the Vega system with zero points from the CALSPEC[9] archive. The total flux of the source within the aperture equals the product Total Counts × PHOTFLAM, where PHOTFLAM is the inverse sensitivity (in erg $cm^{-2}\,s^{-1}\,Å^{-1}$ and representing a signal of 1 electron per second). For WFC3/UVIS images, we adopted the values of the PHOTFLAM keyword in the image headers. However, for the ACS/WFC polarizer images, which were corrected for the throughputs of the polarizers to generate the intensity maps, we discarded the default PHOTFLAM values. Instead, we adopted the most up-to-date PHOTFLAM values in the ACS filter bands for images obtained without polarizers (Bohlin 2012). This is required by the mismatch between (i) the polarizer throughput curves used by SYNPHOT[10] for unpolarized sources and (ii) the values found by comparing unpolarized sources in both the polarizing and nonpolarizing filters (Cracraft & Sparks 2007). Therefore, the PHOTFLAM keywords in ACS/WFC polarized images are not applicable to intensity maps derived from polarized images. Polarization properties of SN 2014J will be discussed in a separate paper (Y. Yang et al. 2016, in preparation).

3.2. Residual Images

Two main echo components are evident. In Figure 4 we show a luminous quarter-circle arc and a diffuse ring at angular distance larger than $0\farcs3$ from the SN. Closer to the SN, uncertainties in the PSF correction prevent reliable detections. On +277 d, the most notable features of the light echoes in $F475W$ are three luminous clumps at angular radius $\alpha = 0\farcs60$ and PAs 80°, 120°, and 150°, measured from north (0°) through east (90°). These clumpy structures are already present on +216 d at the same PAs, but appear smoother and more extended. They eventually evolve into a fairly continuous luminous quarter-circle arc seen on both +365 d and +416 d extending from PA = 60°–170°. Images obtained on +216 d with $F438W$ and $F555W$ show the luminous arc at angular radii $\alpha = 0\farcs54$ and $\alpha = 0\farcs69$, over roughly the same range in PA, in agreement with Crotts (2015). However, for the arc we find a foreground distance of the scattering material that ranges from 226 to 235 pc in the four epochs (Table 4) and has a mean value of 228 ± 7 pc. This is different from the foreground distance of ∼330 pc discussed for this prominent echo component by Crotts (2015). This discrepancy may be due to the difficulties and uncertainties in subtracting the PSF in earlier epoch when the SN is still bright, or in distinguishing the multiple light-echo components identified in our multi-epoch data.

To enable a more quantitative description of the light echoes and their evolution, we performed photometry on them in backgound-subtracted images (Figure 4). We measured the surface brightness of the light-echo profile at different radii and over different ranges in PA. Fan-shaped apertures centered on the SN were used to sample the intensity. The width in PA of each aperture is 45°. In contrast to the luminous arc, the diffuse echo can be seen over the full range in PA from 0° to 360°, but it does not exhibit a common radial profile (Figures 5 and 6).

In the following subsections, we use these measurements to investigate the evolving profile of the light echoes, conduct geometric and photometric analyses, and estimate the dust distribution and scattering properties responsible for the observed light echoes along and close to the DLOS. A function characterizing the properties of the scattering material is constructed to represent the brightness evolution of the observed light echoes on +277 d and +416 d.

3.3. Geometric Properties of the Light Echoes

A comprehensive discussion of the formation of light-echo arcs is available from Tylenda (2004). In the context of this paper, it is sufficient to recall that a circular light echo is created from the intersection of the dust slab with the iso-delay parabaloid. Any uneven distribution of material in the slab results in an uneven flux distribution along the circle, and the light echo may be composed of incomplete arcs. A dust slab always produces a (complete or incomplete) circular light echo, regardless of its inclination with respect to the line of sight. When a dust slab is not perpendicular to the line of sight, the center of the light-echo circle will not coincide with the SN position, and it moves with time.

The luminous arc echo is unresolved with a full width at half maximum of the radial profile approximately that of the SN measured in the same images, i.e., $\sim0\farcs1$ (2 pixels). Therefore, we consider that the luminous arc was formed by a thin dust slab intersecting the line of sight. We have fitted circles to the positions of the luminous arc at all available epochs. None of them are significantly decentered from the SN. This implies

[9] http://www.stsci.edu/hst/observatory/cdbs/calspec.html, or http://www.stsci.edu/hst/acs/analysis/zeropoints/#vega and http://www.stsci.edu/hst/wfc3/phot_zp_lbn
[10] http://www.stsci.edu/institute/software_hardware/stsdas/synphot

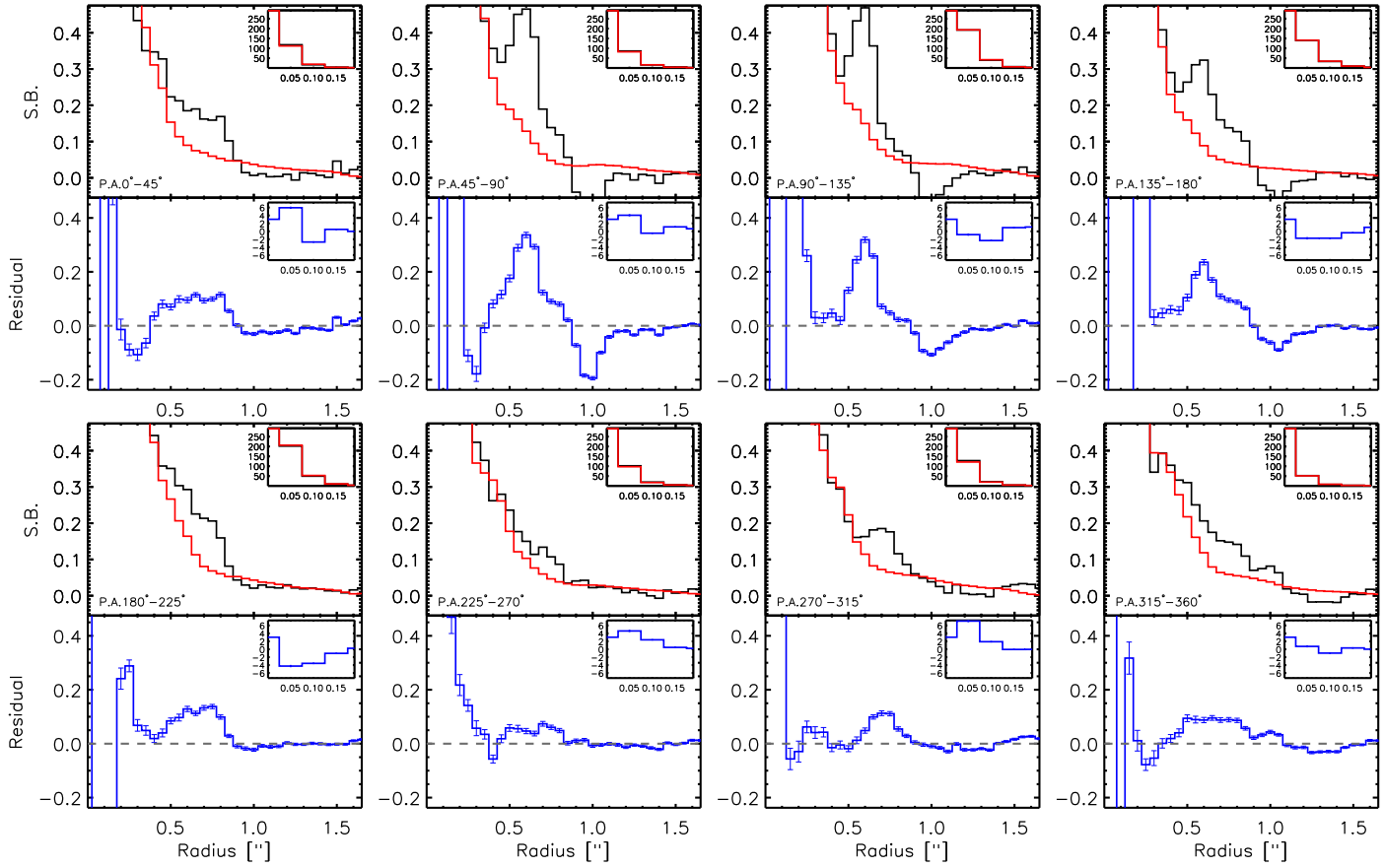

Figure 5. *F475W* band radial surface-brightness profile centered on SN 2014J at 277 days after *B*-band maximum. Different curves in each panel show the surface brightness of the background-subtracted image (black), the TinyTim PSF (red), and the residual after PSF subtraction (blue). Each panel depicts a different 45° sector in PA as labeled. The lower subpanels of each pair display the residuals after PSF and background subtraction; the luminous arc at ~0.6 arcsec is prominent in the PA bins from 45° to 180°. The diffuse light echoes can be identified at other PAs by continuous positive signals from the early epoch of +277 d and continuous negative signals that are due to the subtraction of the intensity map on +796 d. Surface brightnesses are in units of 10^{-16} erg s^{-1} Å^{-1} arcsec^{-2}. The insets display the radial run of the functions (identified by their colors) over the innermost 0.2 arcsec.

that the dust slab producing the arc echo is fairly perpendicular to the line of sight. Table 4 summarizes the geometric properties measured from the luminous arc.

In addition to the luminous arc, a radially extended and diffuse structure is identified, which on +277 d is present in *F475W* and *F606W* and spread over $\alpha = 0\farcs40$ to $\alpha = 0\farcs90$. This structure can also be noted on +365 d in *F438W* and *F555W* (from $\alpha = 0\farcs47$ to $\alpha = 1\farcs03$). It appears more clearly on +416/417 d in *F475W* and *F606W* (from $\alpha = 0\farcs50$ to $\alpha = 1\farcs08$) because for these observations longer exposure times were used. The epochs of observation and the exclusion of the inner $0\farcs3$ limit the explored foreground distances from $z = 100$ pc to $z = 500$ pc. On +216 d, the diffuse component cannot be identified in *F438W,* but is marginally seen in *F555W*. However, the inner and outer radii of the diffuse structure cannot be well determined because of uncertainties in the PSF subtraction. The diffuse light echo observed on +277 d can be produced by a dust cloud intersecting the iso-delay surface over a wide range in foreground distance. The line-of-sight extent of this diffuse dust cloud is indicated by the filled profile of the echoes. This shows that a continuous dust distribution over a certain range of foreground distances along the line of sight is required.

In each panel of the radial profiles in Figures 5 and 6, the radially resolved positive flux excesses (on +277 d and +416 d), and also the radially extended negative flux that is due to the subtraction of the light echo on +796 d, suggest the presence of an extended and inhomogeneous foreground dust distribution. Outside the $\sim 0\farcs3$ region, as discussed earlier, the imperfect PSF subtraction makes the detection of echoes unreliable. The most prominent structure with an intensity peak at the second and third curve near the top in Figure 5 can be clearly seen on +277 d with an angular radius of $\sim 0\farcs60$, which at the distance of M82 (3.53 ± 0.04 Mpc, Dalcanton et al. 2009) is at a radius $\rho = 10.3$ pc from the SN in the plane of the sky. By +416 d, the radius has increased to $\sim 0\farcs735$ or $\rho = 12.6$ pc from the SN. The scattering angles are $2\fdg6$ and $3\fdg2$, respectively.

3.4. Light-echo Mapping of the Foreground Dust Distribution

To our knowledge, and with the exception of SN 1987A in the Large Magellanic Cloud (Crotts 1988; Suntzeff et al. 1988), this is the first radially extended light echo detected from any SN. For epochs discussed in this paper, the diffuse echo component around SN 2014J reveals the SN-backlit ISM over ~40 pc × 40 pc around the DLOS. Standard methods for estimating the optical properties of the ISM toward the supernova only consider the extinction along the DLOS. They include the spectrophotometric comparison between the observed SN and an unreddened SN or template, and comparing the integrated echo flux with the surface brightness

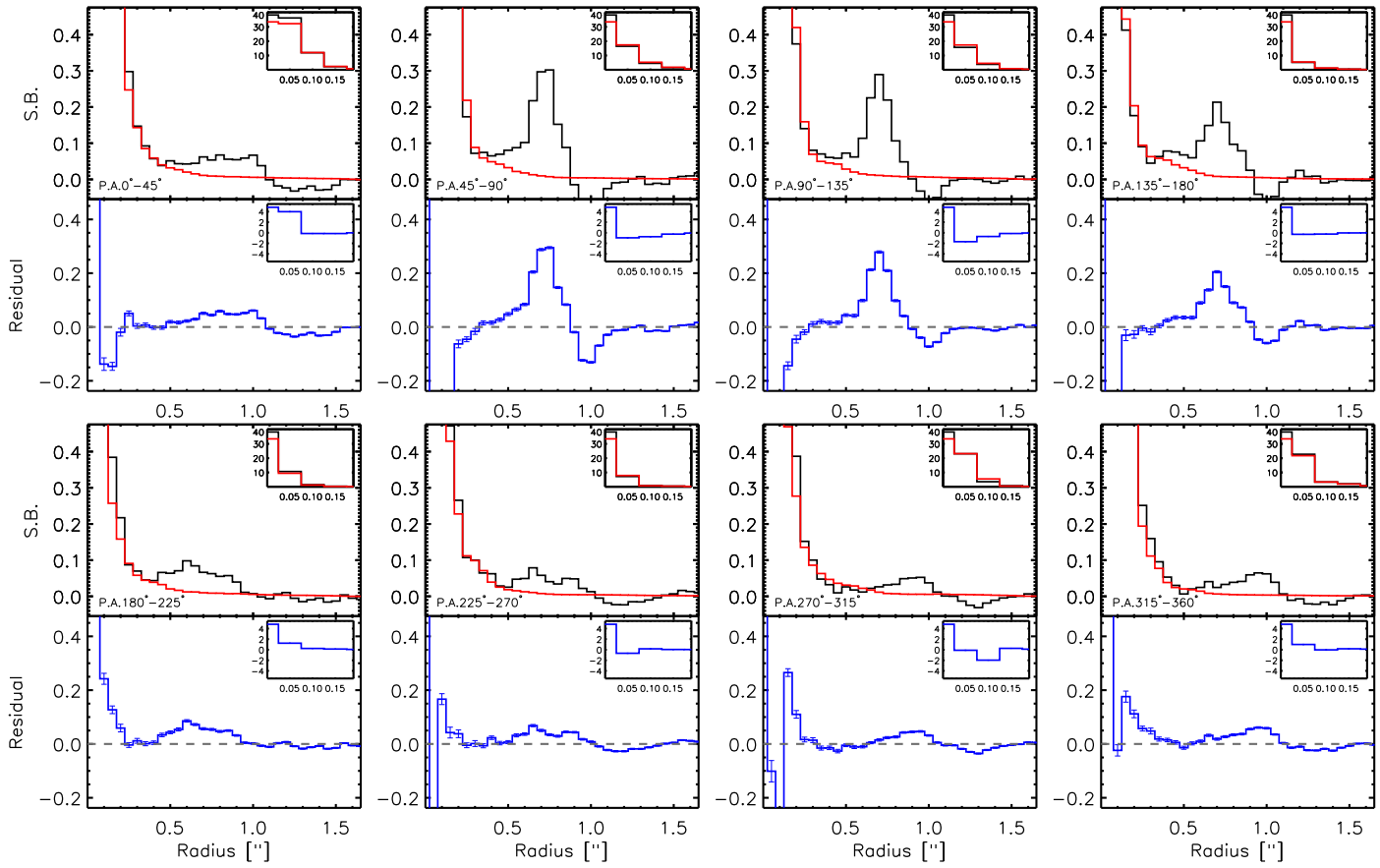

Figure 6. Same as Figure 5, but for the epoch of +416 d.

calculated from the scattering properties of various dust models. The resolved dust echoes of SN 2014J and their temporal evolution in the gas-rich and very nearby galaxy M82, however, provide an unprecedented opportunity to do better. In the following, we take advantage of this to measure the scattering properties of the ISM at different foreground distances and PAs relative to SN 2014J.

We assume that dust scattering follows the Henyey–Greenstein phase function (Henyey & Greenstein 1941):

$$\Phi(\theta) = \frac{1 - g^2}{(1 + g^2 - 2g\cos\theta)^{3/2}}, \quad (4)$$

where $g = \overline{\cos\theta}$ is a measure of the degree of forward scattering. With $L_\lambda(t)$ as the number of photons emitted per unit time by the SN at a given wavelength, $F_\lambda(t) = L_\lambda(t)/4\pi D^2$ is the number of photons observed at time t. D is the distance to the SN. For the modeling of our observations, t is the time of the light-echo observation, t_e denotes the time when photons emitted by the SN would be directly observed along the DLOS, and $F_\lambda(t - t_e)$ is the brightness of the SN at $(t - t_e)$. At t, the photons emitted at the same time as t_e, but experiencing scattering leading to a light echo, arrive at the observer with a time delay $(t - t_e)$.

For a single short flash of light of duration Δt_e emitted by the SN at t_e, $F_\nu(t - t_e) = 0$ for $t \neq t_e$ and $\int_0^t F_\nu(t - t_e)dt_e = F_\nu(t - t_e)|_{t=t_e}\Delta t_e$. Then, the surface brightness, Σ, of a scattered light-echo at frequency ν and arising from an infinitely short (δ function) light pulse is given by

$$\Sigma_\nu^\delta(\rho, \phi, t) = n_d Q_s \sigma_d \frac{F_\nu(t - t_e)|_{t=t_e}\Delta t_e}{4\pi r^2} \left|\frac{dz}{dt}\right| \Phi(\theta)$$
$$= n_d Q_s \sigma_d \frac{\int_0^t F_\nu(t - t_e)dt_e}{4\pi r^2} \left|\frac{dz}{dt}\right| \Phi(\theta). \quad (5)$$

Here n_d is the volume number density of the scattering material in units of cm^{-3}; Q_s is a dimensionless number describing the scattering efficiency of the dust grains; σ_d is the geometric cross section of a dust grain, $\Phi(\theta)$ is the unitless scattering phase function. This means that the surface brightness at a certain instance of the light echo at $t = t_e + (t - t_e)$ is determined by the flux emitted from the SN at t_e, together with the local geometric properties of the iso-delay surface at $t - t_e$.

In reality, the SN emission has a finite duration. $F_\nu(t - t_e)$ is no longer a δ function, and the surface brightness of the light echo unit at a certain frequency Σ_ν is the time integral of $F_\nu(t - t_e)$ from 0 to t:

$$\Sigma_\nu(\rho, \phi, t) = \frac{Q_s\sigma_d}{4\pi}\int_0^t \frac{n_d F_\nu(t - t_e)dt_e}{r^2} \left|\frac{dz}{dt}\right| \Phi(\theta). \quad (6)$$

By recalling that

$$z = \frac{\rho^2}{2ct} - \frac{ct}{2}, \quad (7)$$

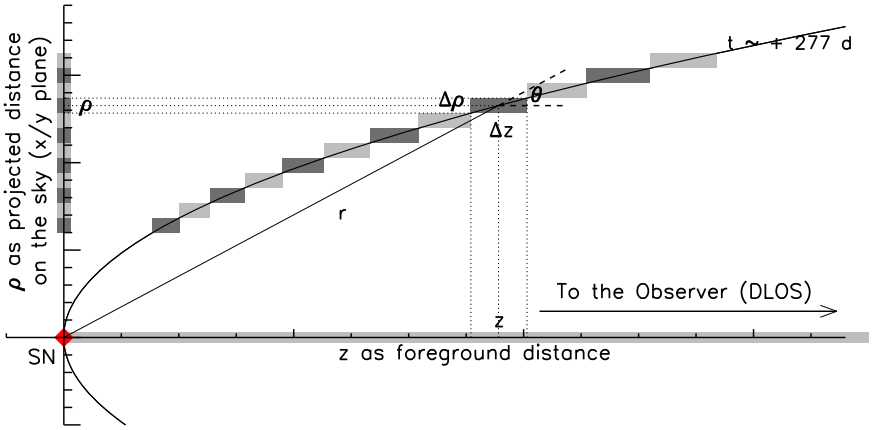

Figure 7. Schematic diagram from Figure 1 adapted to real scale. The paraboloid represents the iso-delay light surface at ~277 d. The gray-shaded squares on the vertical axis indicate the pixelation of echo signals measured from images of this epoch. Rectangles at the same observed angular distance delineate the range in z, over which dust can produce an unresolved light echo. Different gray levels serve to distinguish immediately neighboring pixels.

one can easily find

$$\frac{dz}{dt} = -\frac{c}{2}\left(\frac{\rho^2}{c^2t^2} + 1\right),\ r = z + ct = \frac{ct}{2}\left(\frac{\rho^2}{c^2t^2} + 1\right). \quad (8)$$

Therefore,

$$\Sigma_\nu(\rho, \phi, t) = \frac{Q_s \sigma_d c}{2\pi} \int_0^t \frac{n_d(\rho, \phi, t)}{c^2t^2 + \rho^2} \Phi(\theta)\, F_\nu(t - t_e) dt_e. \quad (9)$$

Because of the relative proximity of M82, some light echoes around SN 2014J are resolved by *HST* at late phases, and each pixel represents the surface brightness of the light echo multiplied by the physical area covered by the pixel in the sky.

Therefore, in order to compare the model flux distribution with the flux in a two-dimensional image, one needs to integrate the model flux over the physical depth covered by the pixel. Since each pixel has size $\Delta x \Delta y$, and $\Delta x = \Delta y$, this implies

$$\mathrm{Im}_\nu(x, y, t) = \int_{x-\frac{\Delta x}{2}}^{x+\frac{\Delta x}{2}} \int_{y-\frac{\Delta y}{2}}^{y+\frac{\Delta y}{2}} \Sigma(x, y, t) dx dy. \quad (10)$$

The geometric factor is determined by the radial distance to the SN, $\rho = \sqrt{x^2 + y^2}$. Therefore, in the tangential direction inside each pixel, we approximate the integration by assuming that n_d (x, y, t) is invariant over the angle $\Delta\phi$ subtended by a single pixel. Furthermore, the angular size of each ACS/WFC pixel is $0\farcs05$. At the distance of $D = 3.53 \pm 0.04$ Mpc, the corresponding physical pixel size in the sky is

$$\begin{aligned} \mathrm{pixscale} &= (3.53 \pm 0.04)\ \mathrm{Mpc} \times \tan(0\farcs05) \\ &= (0.86 \pm 0.01)\ \mathrm{pc} = \Delta x = \Delta y. \end{aligned} \quad (11)$$

We recall the geometric configuration of the iso-delay light surface at +277 d presented by Figure 1. In Figure 7 we modify this schematic diagram to demonstrate how we use a two-dimensional image to map the ISM in three dimensions. The gray-shaded fields on the vertical axis show the pixelation of the sky view by the camera, with each pixel measuring 0.86 pc on both sides. Δz is the position-dependent line-of-sight extent of the foreground column covered by each pixel. Gray-shaded rectangles superimposed on the iso-delay light surface mark columns of ISM that would be responsible for the respective light echoes as projected onto the sky. The fixed size of the sky pixels leads to varied lengths of the foreground columns of ISM. If the ISM is homogeneously distributed in the x/y plane, then the total per-sky-pixel extinction of the scattering materials as revealed by the light echo can be estimated by summing the extinction along each rectangular column of ISM intersecting the iso-delay light paraboloid. Comparison of the extinction by the scattering materials to the extinction along the DLOS (marked by the gray line on the z-axis in Figure 7) may reveal whether they are caused by the same dust mixture and perhaps even the same dust cloud.

Now we can compare the intensity map obtained from the observations with the light echo modeled at each physical position for a given time t of the observation as follows:

$$\begin{aligned} \mathrm{Im}_\nu(x, y, t) = \frac{\omega C_{\mathrm{ext}} c}{2\pi} \Delta x \int_{x-\frac{\Delta x}{2}}^{x+\frac{\Delta x}{2}} dx \int_0^t \frac{n_d(x, y, t)}{c^2t^2 + \rho^2} \\ \times \Phi(\theta) F_\nu(t - t_e) dt_e. \end{aligned} \quad (12)$$

3.5. Extinction of the Scattering Materials

The optical properties of the dust grains that are responsible for the light echoes around SN 2014J can be deduced within each observed pixel. We estimate the extinction properties of the scattering materials based on an approach that combines single scattering with attenuation (see Section 5 of Patat 2005 for more details). Conversions from the intensity map to the number-density map ("nd") are presented by Figure 8 based on Equation (12). We follow the sampling in Figures 5 and 6 and present the deduced optical properties of the dust grains for the PA sector 45°–90°, which includes the brightest part of the luminous arc, and PA sector 315°–360°, which covers the diffuse echo ring observed with the highest S/N. They are shown in Figure 9 for *F475W* and Figure 10 for *F606W*, both on +277 d. In these diagrams, the rectangular coordinates x and y are replaced with the polar coordinates ρ and ϕ, and the abscissa corresponds to the physical distances in the plane of the sky. The left ordinate represents the quantity $\omega C_{\mathrm{ext}} n_d(\rho, \phi, t)$, which is determined by the optical properties of the dust grains. The right ordinate shows $\omega C_{\mathrm{ext}} n_d dz = \omega\tau$, where τ is the optical depth of the dust mapped onto a single pixel. By looking at the entire echo profile, we found that a major part of the luminous-arc echo spreads over 45°–180° in PA, and the diffuse echo ring attained the highest S/N over 270°–360° in PA.

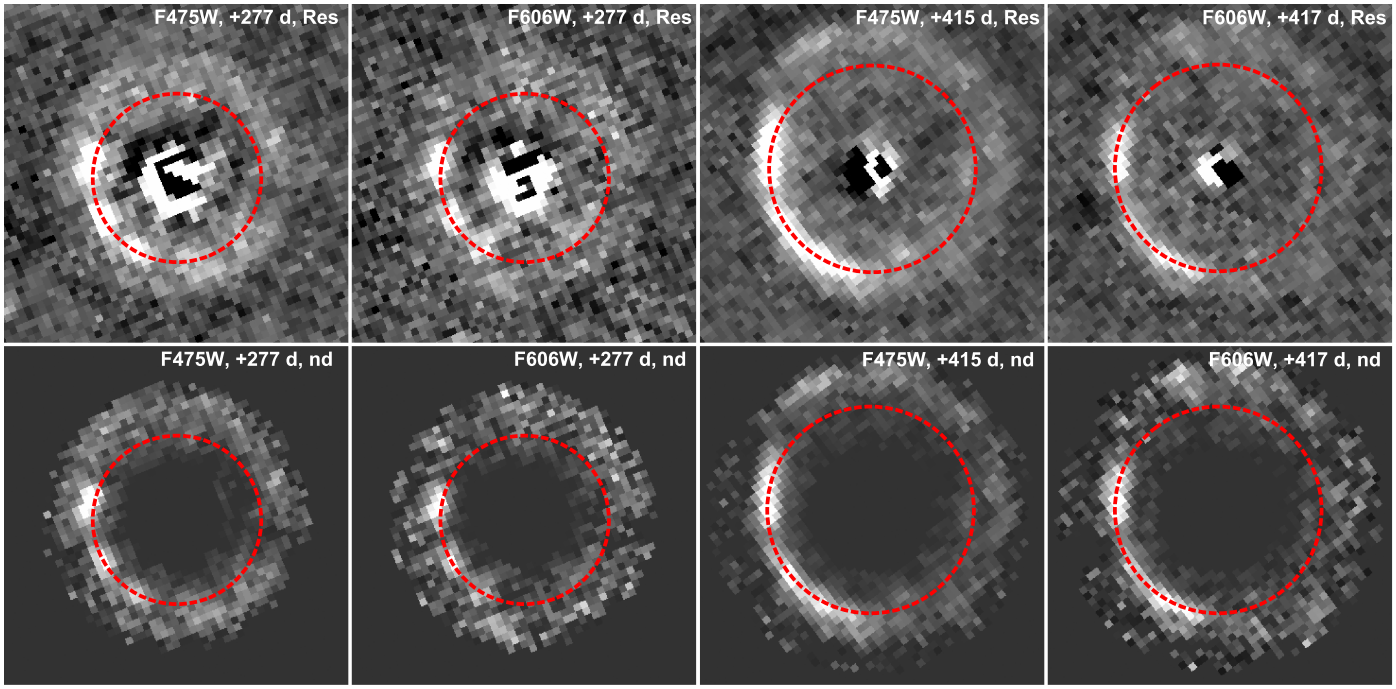

Figure 8. Intensity maps of the backgound- and PSF-subtracted images (labeled "Res") and scaled volume number-density maps ("nd") showing the relative column density calculated from the flux and location in space of each pixel. North is up and east is left. Epoch and passband of the observations are labeled. Dashed circles trace the dust slab at $z \sim 228$ pc, which is responsible for the luminous echo arc appearing with different diameter at different epochs. Overdensities can be identified at PAs 60°–180° along the lunimous arc and also at PAs 0°–60° and larger radii in *F475W* and *F606W* +416/+417 d.

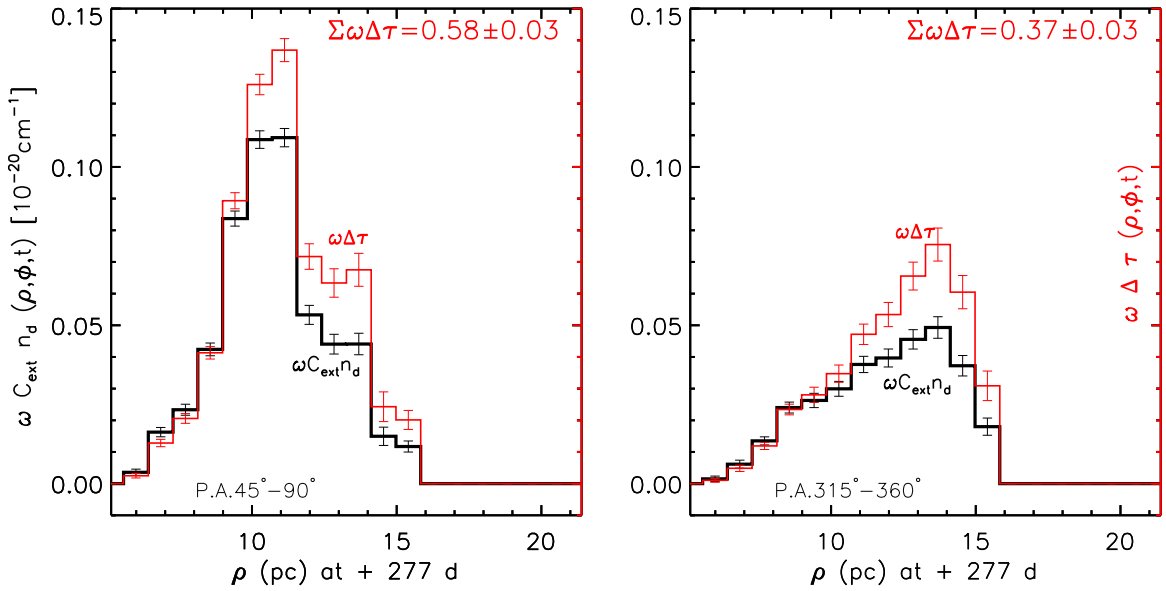

Figure 9. Radial profiles at different PAs (as labeled) of optical properties of the scattering material. The calculations are based on the density map (transformed from the residual image) in passband *F475W* on +277 d. The left panel shows the luminous arc echo, and the right panel presents the diffuse ring echo. The *x*-axis shows the physical distances in the plane of the sky (ρ-direction). Black histograms represent $\omega C_{\rm ext} n_d(\rho, \phi, t)$ in units of 10^{-20} cm^{-1} as shown on the left ordinate and can be used to infer the volume densities. Red histograms represent the dimensonless $\omega C_{\rm ext} n_d dz = \omega\tau$ and share the tick marks of the left ordinate, from which column number densities can be deduced. The optical depth of the dust mapped onto a single pixel gives τ.

(An extended version of this figure is available.)

We applied a Galactic extinction model with $R_V = 3.1$ to the scattering materials and compare the reproduced extinction properties with the extinction along the DLOS. Discrepancies between the derived quantities and the assumed model will indicate that the extinction properties of the scattering dust are different from the Milky Way dust with $R_V = 3.1$. For each photometric bandpass its pivot wavelength was used in interpreting the parameters from dust models. The extinction curve is obtained from Weingartner & Draine (2001) and Draine (2003a, 2003b).[11] For $C_{\rm ext}$, the extinction cross section per hydrogen nucleon H, we adopted 5.8×10^{-22} cm^2/H for *F475W*, and 4.4×10^{-22} cm^2/H for *F606W*; for the scattering

[11] ftp://ftp.astro.princeton.edu/draine/dust/mix/kext_albedo_WD_MW_3.1_60_D03.all

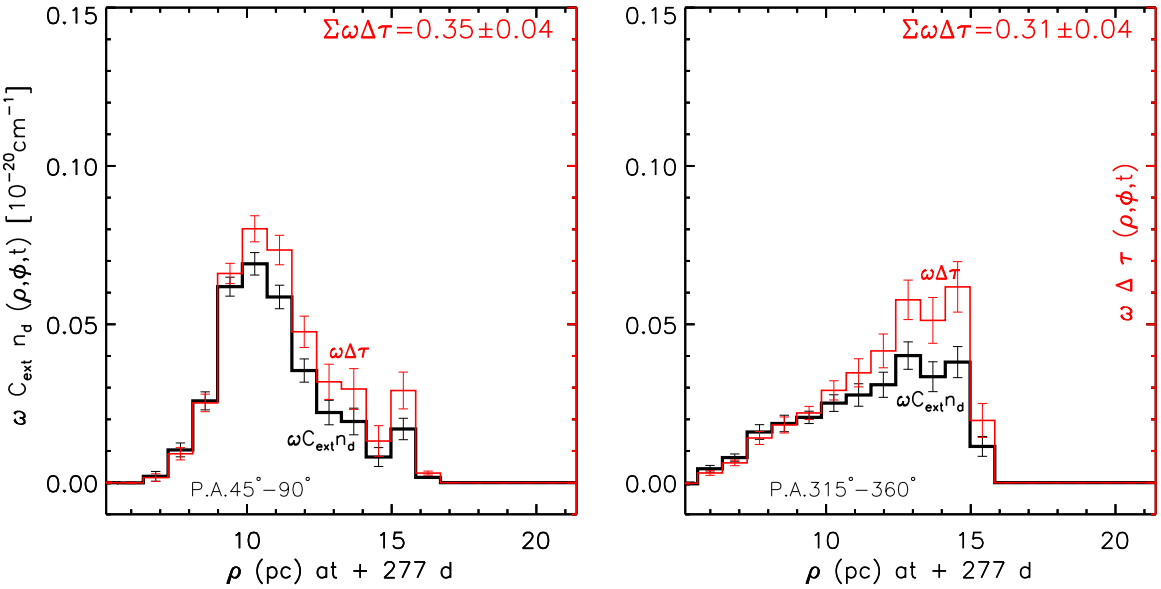

Figure 10. Same as Figure 9, but for *F606W*.
(An extended version of this figure is available.)

phase function, we adopted $g = 0.555$ for *F475W*, and $g = 0.522$ for *F606W*, and n_d is the H volume number density in units of cm^{-3}.

For a uniform dust distribution in the x/y direction (in the plane of the sky), integrating $\omega\tau$ over each position angle will provide a rough estimate of the product of the total optical depth and the scattering albedo, which is the main value added by the separate analysis of light echoes. We applied the same extinction measured along the DLOS to the scattered light-echoes and calculated the optical depth of the materials from scattering. This is labeled by the red text in the upper right of each panel of Figures 9 and 10. The inhomogeneity of the ISM in M82 has small scales, as is indicated by the rapid variability of the strength of the echo with PA along the rings as well as with time. The optical depth along the DLOS has been measured by Foley et al. (2014) around maximum light as $\tau_B = 3.11(0.18)$ and $\tau_V = 1.91(0.17)$ based on $A_B = 3.38(20)$, $A_V = 2.07(18)$ and using the relation $A_\lambda = -2.5\log_{10}(e)\,\tau_\lambda^{\mathrm{ext}} = 1.086\tau_\lambda^{\mathrm{ext}}$.

The hydrogen column number density along the line of sight is $n_H = \int_{\mathrm{LOS}} n_d(z)dz$. Therefore, n_H can be obtained by dividing the total optical depth per bin in position angle by ωC_{ext} (Figure 9 for *F475W* and Figure 10 for *F606W*). For example, for *F475W* and +277 d, the maximum value of $\omega\tau$ (ρ, ϕ, t) in the luminous arc was observed to be around 0.58. Using $\omega \sim 0.65$ for the Milky Way dust model with $R_V = 3.1$ given by Weingartner & Draine (2001), n_H can be estimated to be $n_H = 0.58/\omega C_{\mathrm{ext}} = 0.58/\ (0.65 \times 5.8 \times 10^{-22}\,\mathrm{cm}^2/\mathrm{H}) \sim 1.5 \times 10^{21}$ H cm^{-2} in the bin that shows the densest part of the dust slab producing the luminous arc echo. This is ~15 times denser than the scattering material in the foreground of the Type II plateau SN 2008bk (Van Dyk 2013), for which the visual extinction of the dust responsible for the echo is $A_V \approx 0.05$. It is also ~4 times denser than the ISM in the foreground of the Type II plateau SN 2012aw (Van Dyk et al. 2015), for which the dust extinction in the SN environment responsible for the echo is consistent with the value that was estimated from observations of the SN itself at early times, i.e., $A_V = 0.24$.

3.6. Scattering Wavelength Dependence of the ISM

From the scattering properties of the dust, its optical properties can be estimated by comparing the quantity $\omega C_{\mathrm{ext}} n_d$ derived for *F475W* and *F606W*. Figure 11 presents the division of the profiles of Figure 9 by Figure 10. This yields the wavelength dependence of the extinction cross section. As the ordinate of Figure 11 we use $\omega\tau_{F475W}/\omega\tau_{F606W}$. Overplotted histograms show (in red) the number density of the scattering material derived from the strength of the echoes in *F475W*. The horizontal gray dashed lines mark the value of $\tau_{F475W}/\tau_{F606W} = A_{F475W}/A_{F606W} = 1.66$, 1.30, and 1.19 for Milky Way-like dust with $R_V = 1.4$, 3.1, and 5.5, respectively, according to the algorithm determined by Cardelli et al. (1989). For completeness, extended versions of Figures 9, 10, and 11 over the entire eight bins of PA are available in the online journal.

Plausible estimates of $\omega\tau_{F475W}/\omega\tau_{F606W}$ can only be made in regions of the echoes with high S/N. In the left panel of Figure 11, the luminous arc at $\rho = 10 \sim 11$ pc has an average value $\omega\tau_{F475W}/\omega\tau_{F606W} \sim 1.7$ (dimensionless), shown by the black histograms. For the diffuse structure, the right panel indicates an average value ~1.3. This difference in the wavelength dependence measured from the scattering optical depth indicates that the size of the grains in the thin dust slab producing the luminous arc is different from the grain sizes in the foreground extended dust cloud producing the diffuse echo. While this difference is significant, one should be cautious about the inferred absolute values of R_V in this approach, considering the low S/N and the large uncertainties.

Figure 12 presents the three-dimensional dust distribution estimated for SN 2014J. Data points show the number densities as derived from two iso-delay paraboloids. Scattering materials producing the luminous arc and the diffuse echo were mapped

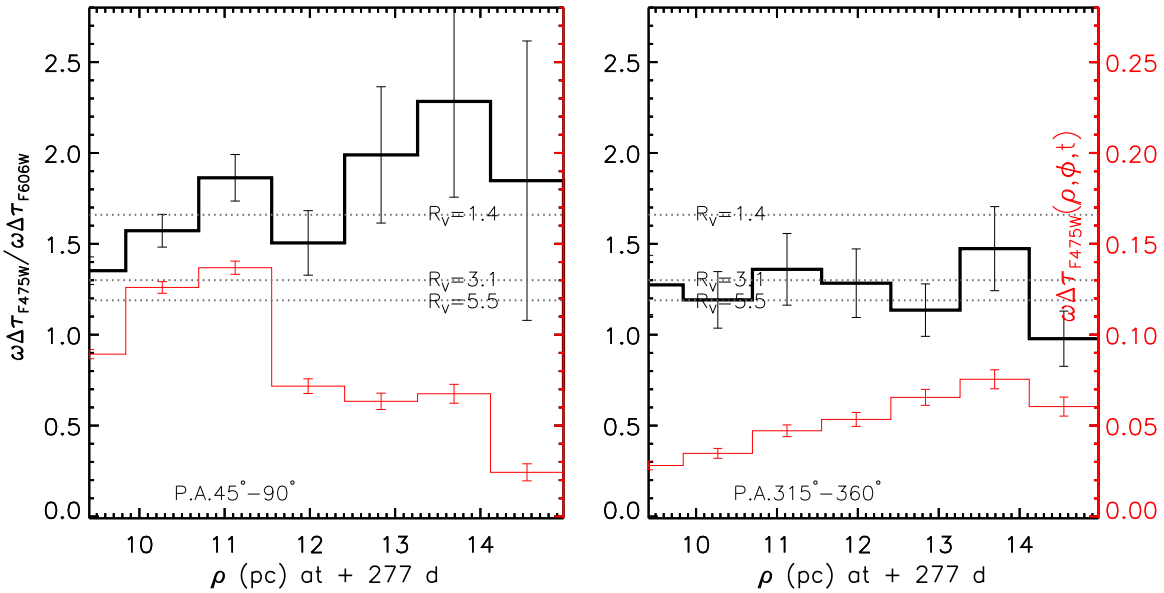

Figure 11. Radial run of the wavelength dependence of the scattering material characterized by $\omega\tau_{F475W}/\omega\tau_{F606W}$ on +277 d, shown by the black histograms. Red histograms represent the dimensionless quantity $\omega C_{\rm ext} n_d dz = \omega\tau$, which is a measure of the strength of the echoes. The abscissa measures the physical distances (in pc) in the plane of the sky. The upper, middle, and lower horizontal dashed lines represent the values calculated for Milky Way extinction laws with $R_V = 1.4$, 3.1, and 5.5, respectively. The left panel includes the luminous arc echo at $\rho = 10 \sim 11$ pc and $\omega\tau_{F475W}/\omega\tau_{F606W} \sim 1.7$. The right panel presents the diffuse ring echo, exposing a different wavelength dependence of scattering with $\omega\tau_{F475W}/\omega\tau_{F606W} \sim 1.3$.

(An extended version of this figure is available.)

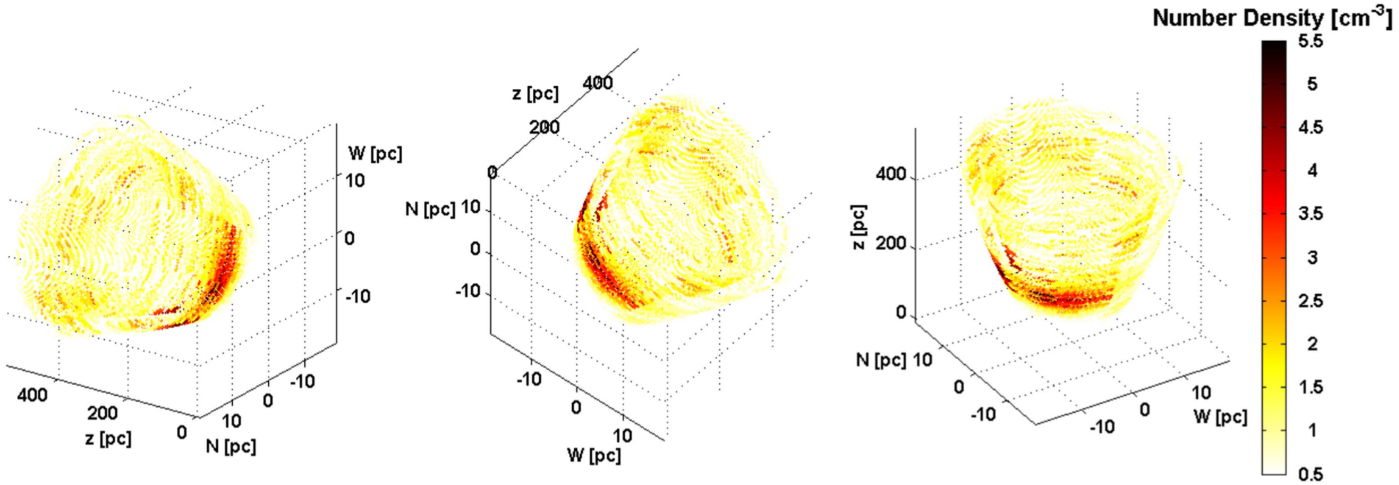

Figure 12. The three-dimensional dust distribution derived from the light echoes around SN 2014J. From left to right, the vertical axis corresponds to the directions east–west, north–south, and the DLOS (z). The color encoding of the number density of the dust is indicated by the vertical bar. The measurements map out density along iso-delay paraboloids as schematically depicted in Figure 1. They correspond to epochs +277 d and +416 d and are too close to one another to appear separately.

out at epochs +277 d (inner layer) and +416 d (outer layer), respectively.

4. DISCUSSION

The diffuse echo component favors a higher R_V than the luminous arc, corresponding to a less steep wavelength dependence of the extinction in the diffuse echo compared to the luminous arc. In general terms, this implies that the grains in the dust slab producing the luminous arc are smaller than those in the extended, diffuse ISM. The R_V value measured from the diffuse echo at $\rho \sim 10$–14 pc to the position of SN 2014J, i.e., $R_V \sim 3$, is close to that found by Hutton et al. (2015) by modeling the attenuation law based on near-ultraviolet and optical photometry of M82 at large. Accordingly, the dust grains in the extended foreground ISM producing the diffuse echo ring are similar in size to those in the Milky Way. Extinction in the luminous arc, however, favors a lower R_V value, similar to the extinction law deduced from the SN itself, represented by $R_V \sim 1.4$. This similarity indicates that the grain size distribution in the slab of the ISM producing the luminous arc is similar to the ISM responsible for the extinction measured toward the SN at early epochs.

The optical depth due to light scattered by the ISM can be estimated as follows. If they have similar properties as Milky Way-like dust with $R_V = 3.1$, τ_{F475W} ranges from 0.3 at PA 225°–270°, covering part of the diffuse ring, to 0.9 at PA 45°–90°, where the luminous arc is brightest. These optical depths are lower than the depth along the DLOS. One possible

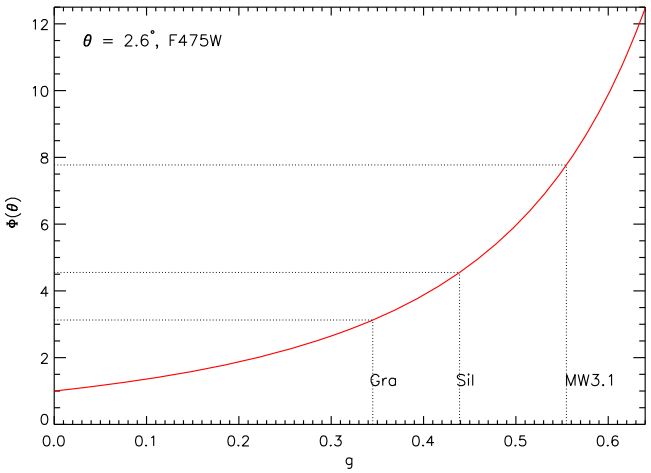

Figure 13. Fraction of light scattered at the small angle of 2.°6 as a function of the value of the phase scattering function, g, as calculated from Equation (4). MW3.1, Gra, and Sil represent the g factors for Milky Way dust with $R_V = 3.1$, graphite spheres with radius 0.1 μm, and "astronomical silicate" spheres with radius 0.1 μm.

explanation for the discrepancy can be an overestimate of the degree of forward scattering. At +277 d, the scattering angle is ~2.°6 for the luminous arc-producing dust. A dramatic increase in forward scattering occurs with increasing grain size, while smaller grains scatter light more isotropically, leading to a lower value of the phase function, see Chapter 5 of van de Hulst (1957). Therefore, to produce a light echo of the same strength, smaller dust grains in the ISM responsible for the luminous arc require a higher optical depth than larger Milky Way-like dust grains.

To illustrate the dependence of the degree of forward scattering on the optical depth, we investigate the Heyney–Greenstein phase function characterizing the angular distribution of scattered light intensity as shown by Equation (4). Figure 13 demonstrates the fraction of scattered light at small scattering angle, i.e., 2.°6 as a function of scattering asymmetry factor, g. In this figure, values of $g = 0.439$ and $g = 0.345$ are indicated for astronomical silicate and graphite grains with radius of 0.1 μm according to calculations based on Draine & Lee (1984) and Laor & Draine (1993).

When the grains are significantly smaller than the wavelength of light, the classical Rayleigh scattering limit is reached. The asymmetry factor for Rayleigh scattering is $g = 0$, and the phase function becomes unity, indicating no directional preference of scattering. This is the case for the luminous arc, while the phase function has a value of 7.8 for Milky Way dust with $R_V = 3.1$. This means that the optical depth calculated for the case of Rayleigh scattering is 7.8 times larger than for Milky Way dust with $R_V = 3.1$. The densest part of the scattering material will attain a value of ~7.0 in $F475W$, significantly larger than the optical depth measured along the DLOS. On the other hand, the asymmetry factor g approaches unity for larger grains, and the efficiency of forward scattering increases substantially.

The grain size distribution in the extinction-producing material toward SN 2014J itself is similar to that of the luminous arc-producing material, as inferred from the similarity of R_V found in both of the two ISM components. Considering this low R_V and the lower optical depth found in the scattering material responsible for the luminous arc, we infer that these scattering materials are also responsible for the extinction toward SN 2014J. Our result is consistent with the relationship between the host galaxy extinction A_V and their measured R_V (Mandel et al. 2011), which for SNe with low extinction, $A_V \lesssim 0.4$, $R_V \approx 2.5$–2.9 is favored, while at high extinction, $A_V \gtrsim 1$, low values of $R_V < 2$ are favored. Owing to the lack of knowledge about the detailed distribution and optical properties of the dust in M82, we cannot rule out the possibility that the different extinctions along the scattering line of sight of the materials and the DLOS may partly also be caused by a denser ISM along the DLOS. The extinction along the DLOS may also be due to dust at small foreground distances, which would produce light echoes too close to the SN to be detected. Additionally, it is possible that the extinction can be generated by interstellar dust clouds placed too far in front of the SN. We recall that Equations (8) and (9) showed that the luminosity of the light echo resulting from a dust slab intersecting the DLOS decreases as $1/r$ (where r is the distance between the SN and the dust slab). Considering that numerous Na, Ca, and K features have been seen along the DLOS (Patat et al. 2015), we cannot rule out the possibility that there are dust clouds placed more than 500 pc away from the SN and that they can hardly be detected in current images.

The smaller grains found in the dense dust slab seem to be inconsistent with the grain size distribution in dense regions inferred by Cardelli et al. (1989) and Whittet et al. (1992), who offered the qualitative explanation that coagulation inside the dense interstellar dust clouds removes the smaller particles and results in higher R_V. It is possible that the dense dust slab and the porous diffuse dust cloud belong to different components of the ISM, which are formed by different mechanisms and at significantly different episodes of the history of M82. For instance, considering the possibility that the dense dust slab that produced the luminous arc echo was formed more recently, i.e., around an episode of intense star formation at ~60 Myr ago (Gallagher & Smith 1999), the size growth may not be significant in the dense dust slab considering the relatively long time of the grain growth, i.e., see Figure 8 of Mattsson (2016).

The presented light-echo model is necessarily only a simplified approximation of reality. Our model attempts to reproduce the optical depth of the scattering material over a projected area of ~40 pc × 40 pc in the plane of the sky and compares it to the optical depth measured for the DLOS. One major source of uncertainty is the assumption of single scattering (Wood et al. 1996; Patat 2005). In view of the large extinction measured toward SN 2014J, a Monte Carlo simulation with various grain size distributions should give a better representation of the real scattering process. Another uncertainty results from using the extinction measured along the DLOS around maximum light for the echo-producing material as well. Additionally, the assumption of Galactic R_V values may not be realistic for M82.

5. SUMMARY

The geometric and photometric evolution of resolved light echoes around SN 2014J was monitored with *HST*. Two main constituents were found. From a luminous arc, a discrete slab of dust was inferred at a foreground distance of 228 ± 7 pc. In addition, a resolved diffuse ring-like light echo implies that another foreground ISM component is widely distributed over distances of ~100–500 pc. If the scattering material suffers the same extinction as along the DLOS, then the densest part has a number density of $\sim 1.5 \times 10^{21}\,\mathrm{cm}^{-2}$, based on an approach

that combines single scattering with attenuation. The scattering material is unevenly distributed with PA. The wavelength dependence of the scattering optical depth is steeper in the luminous arc than in the diffuse ring. The former favors a small $R_V \sim 1.4$, as also measured along the DLOS, and the latter is more consistent with a "normal" $R_V \sim 3$. This suggests that the average grain size is smaller in the ISM and is responsible for the luminous arc, and the more widely distributed scattering materials have average properties similar to Milky Way-like dust. This study reveals the R_V fluctuation of the extragalactic dust on parsec scales. We deduce that systematically steeper extinction laws toward SNe Ia do not have to represent the average behavior of the extinction law in the host galaxy.

The optical depth of the scattering material estimated from the scattering properties of Milky Way-like dust with $R_V = 3.1$ is smaller than the optical depth measured along the DLOS. The optical depth along the DLOS is better reproduced with smaller grains, as also indicated for the dust slab responsible for the luminous arc. This suggests that an extension of this dust slab, or a separate cloud with similar properties, is also responsible for the extinction toward SN 2014J. More data will be collected in future observing campaigns that will help to additionally characterize the extinction laws measured within different light-echo components. Further constraints on the amount and properties of the circumstellar and interstellar material from polarimetry and very late-time photometry will be discussed in future work.

We are grateful to Peter Lundqvist and Anders Nyholm for providing the late-time spectrum of SN 2014J. We also thank Jian Gao, Bi-wei Jiang, Kevin Krisciunas, Armin Rest, and Nicholas Suntzeff for helpful discussions. The supernova research by Y. Yang, P. J. Brown, and L. Wang is supported by NSF grant AST-0708873. P. J. Brown was partially supported by a Mitchell Postdoctoral Fellowship. Y. Yang and M. Cracraft also acknowledge support from NASA/STScI through grants HST-GO-13717.001-A., HST-GO-14139.001-A., and HST-GO-14663.001-A. L. Wang is supported by the Strategic Priority Research Program "The Emergence of Cosmological Structures" of the Chinese Academy of Sciences, Grant No. XDB09000000. L. Wang and X. Wang are supported by the Major State Basic Research Development Program (2013CB834903), and X. Wang is also supported by the National Natural Science Foundation of China (NSFC grants 11178003 and 11325313).

REFERENCES

Amanullah, R., & Goobar, A. 2011, ApJ, 735, 20
Amanullah, R., Goobar, A., Johansson, J., et al. 2014, ApJL, 788, L21
Bohlin, R. C. 2012, Flux Calibration of the ACS CCD Cameras IV. Absolute Fluxes, Instrument Science Report ACS 2012-01, Tech. Rep. (Baltimore, MD: STScI)
Bonanos, A. Z., & Boumis, P. 2016, A&A, 585, A19
Bond, H. E., Gilmozzi, R., Meakes, M. G., & Panagia, N. 1990, ApJL, 354, L49
Bond, H. E., Henden, A., Levay, Z. G., et al. 2003, Natur, 422, 405
Brown, P. J., Smitka, M. T., Wang, L., et al. 2015, ApJ, 805, 74
Bulla, M., Sim, S. A., Pakmor, R., et al. 2016, MNRAS, 455, 1060
Cappellaro, E., Patat, F., Mazzali, P. A., et al. 2001, ApJL, 549, L215
Cardelli, J. A., Clayton, G. C., & Mathis, J. S. 1989, ApJ, 345, 245
Chevalier, R. A. 1986, ApJ, 308, 225
Cikota, A., Deustua, S., & Marleau, F. 2016, ApJ, 819, 152
Cracraft, M., & Sparks, W. B. 2007, ACS Polarization Calibration—Data, Throughput, and Multidrizzle Weighting Schemes, Instrument Science Report ACS 2007-10, Tech. Rep.
Crotts, A. P. S. 1988, ApJL, 333, L51
Crotts, A. P. S. 2015, ApJL, 804, L37
Dalcanton, J. J., Williams, B. F., Seth, A. C., et al. 2009, ApJS, 183, 67
Davidson, K., & Humphreys, R. M. 2012, Natur, 486, E1
Draine, B. T. 2003a, ARA&A, 41, 241
Draine, B. T. 2003b, ApJ, 598, 1017
Draine, B. T., & Lee, H. M. 1984, ApJ, 285, 89
Drozdov, D., Leising, M. D., Milne, P. A., et al. 2015, ApJ, 805, 71
Fitzpatrick, E. L. 1999, PASP, 111, 63
Foley, R. J., Fox, O. D., McCully, C., et al. 2014, MNRAS, 443, 2887
Fossey, J., Cooke, B., Pollack, G., Wilde, M., & Wright, T. 2014, CBET, 3792, 1
Gallagher, J. S., III, & Smith, L. J. 1999, MNRAS, 304, 540
Gao, J., Jiang, B. W., Li, A., Li, J., & Wang, X. 2015, ApJL, 807, L26
Gonzaga, S., Hack, W., Fruchter, A., & Mack, J. 2012, The DrizzlePac Handbook (Baltimore, MD: STScI)
Goobar, A. 2008, ApJL, 686, L103
Goobar, A., Johansson, J., Amanullah, R., et al. 2014, ApJL, 784, L12
Graham, M. L., Valenti, S., Fulton, B. J., et al. 2015, ApJ, 801, 136
Grefenstette, B. W., Harrison, F. A., Boggs, S. E., et al. 2014, Natur, 506, 339
Hartig, G. F. 2009, WFC3 SMOV Programs 11436/8: UVIS On-orbit PSF Evaluation, Instrument Science Report WFC3 2009-38, Tech. Rep. (Baltimore, MD: STScI)
Havlen, R. J. 1972, A&A, 16, 252
Henyey, L. G., & Greenstein, J. L. 1941, ApJ, 93, 70
Hoang, T. 2015, arXiv:1510.01822
Hutton, S., Ferreras, I., & Yershov, V. 2015, MNRAS, 452, 1412
Jack, D., Mittag, M., Schröder, K.-P., et al. 2015, MNRAS, 451, 4104
Johansson, J., Goobar, A., Kasliwal, M. M., et al. 2014, arXiv:1411.3332
Kapteyn, J. C. 1901, AN, 157, 201
Kawabata, K. S., Akitaya, H., Yamanaka, M., et al. 2014, ApJL, 795, L4
Krist, J. 1993, in ASP Conf. Ser. 52, Astronomical Data Analysis Software and Systems II, ed. R. J. Hanisch, R. J. V. Brissenden, & J. Barnes (San Francisco, CA: ASP), 536
Krist, J., & Hook, R. 2008, Tiny Tim Users Manual v6.2, http://www.stsci.edu/software/tinytim/
Laor, A., & Draine, B. T. 1993, ApJ, 402, 441
Liu, J.-F., Bregman, J. N., & Seitzer, P. 2003, ApJ, 582, 919
Lundqvist, P., Nyholm, A., Taddia, F., et al. 2015, A&A, 577, A39
Mandel, K. S., Narayan, G., & Kirshner, R. P. 2011, ApJ, 731, 120
Maund, J. R., & Smartt, S. J. 2005, MNRAS, 360, 288
Mattsson, L. 2016, arXiv:1606.02272
Meikle, W. P. S., Mattila, S., Gerardy, C. L., et al. 2006, ApJ, 649, 332
Otsuka, M., Meixner, M., Panagia, N., et al. 2012, ApJ, 744, 26
Patat, F. 2005, MNRAS, 357, 1161
Patat, F., Benetti, S., Cappellaro, E., & Turatto, M. 2006, MNRAS, 369, 1949
Patat, F., Chandra, P., Chevalier, R., et al. 2007, Sci, 317, 924
Patat, F., Taubenberger, S., Cox, N. L. J., et al. 2015, A&A, 577, A53
Phillips, M. M., Lira, P., Suntzeff, N. B., et al. 1999, AJ, 118, 1766
Porter, A. L., Leising, M. D., Williams, G. G., et al. 2016, ApJ, 828, 24
Quinn, J. L., Garnavich, P. M., Li, W., et al. 2006, ApJ, 652, 512
Rest, A., Matheson, T., Blondin, S., et al. 2008, ApJ, 680, 1137
Rest, A., Prieto, J. L., Walborn, N. R., et al. 2012, Natur, 482, 375
Riess, A. G., Press, W. H., & Kirshner, R. P. 1996, ApJ, 473, 588
Ritchey, G. W. 1901, ApJ, 14, 293
Sand, D. J., Hsiao, E. Y., Banerjee, D. P. K., et al. 2016, ApJL, 822, L16
Schmidt, B. P., Kirshner, R. P., Leibundgut, B., et al. 1994, ApJL, 434, L19
Sinnott, B., Welch, D. L., Rest, A., Sutherland, P. G., & Bergmann, M. 2013, ApJ, 767, 45
Sirianni, M., Jee, M. J., Benítez, N., et al. 2005, PASP, 117, 1049
Sparks, W. B. 1994, ApJ, 433, 19
Sparks, W. B., Macchetto, F., Panagia, N., et al. 1999, ApJ, 523, 585
Spyromilio, J., Malin, D. F., Allen, D. A., Steer, C. J., & Couch, W. J. 1995, MNRAS, 274, 256
Srivastav, S., Ninan, J. P., Kumar, B., et al. 2016, MNRAS, 457, 1000
Sugerman, B., & Lawrence, S. 2016, ATel, 8890
Sugerman, B. E. K. 2003, AJ, 126, 1939
Sugerman, B. E. K. 2005, ApJL, 632, L17
Sugerman, B. E. K., & Crotts, A. P. S. 2002, ApJL, 581, L97
Suntzeff, N. B., Heathcote, S., Weller, W. G., Caldwell, N., & Huchra, J. P. 1988, Natur, 334, 135
Swope, H. H. 1940, BHarO, 913, 11
Tylenda, R. 2004, A&A, 414, 223

van de Hulst, H. C. 1957, Light Scattering by Small Particles (New York: Wiley)
Van Dyk, S. D. 2013, AJ, 146, 24
Van Dyk, S. D., Lee, J. C., Anderson, J., et al. 2015, ApJ, 806, 195
Van Dyk, S. D., Li, W., & Filippenko, A. V. 2006, PASP, 118, 351
Vogt, F. P. A., Besel, M.-A., Krause, O., & Dullemond, C. P. 2012, ApJ, 750, 155
Wang, L. 2005, ApJL, 635, L33
Wang, X., Li, W., Filippenko, A. V., et al. 2008, ApJ, 677, 1060
Weingartner, J. C., & Draine, B. T. 2001, ApJ, 548, 296
Welch, D. L., Clayton, G. C., Campbell, A., et al. 2007, ApJ, 669, 525
Whittet, D. C. B., Martin, P. G., Hough, J. H., et al. 1992, ApJ, 386, 562
Wood, K., Bjorkman, J. E., Whitney, B. A., & Code, A. D. 1996, ApJ, 461, 828
Xu, J., Crotts, A. P. S., & Kunkel, W. E. 1994, ApJ, 435, 274
Zheng, W., Shivvers, I., Filippenko, A. V., et al. 2014, ApJL, 783, L24